Grid Frequency Regulation Based on Point of Common Coupling Angle Deviation Control of Distributed Energy Resources With Fully Active Hybrid Energy Storage System

Aniket Joshi, *Student Member, IEEE*, Arun Suresh, *Student Member, IEEE*, and Sukumar Kamalasadan, *Senior Member, IEEE*

***Abstract*—This article proposes an architecture that controls hybrid energy storage system (HESS) integrated photovoltaic distributed energy resource (as a dc-microgrid) and achieves grid frequency regulation by capturing voltage angle deviations ($\Delta\delta$) at the microgrid point of common coupling (PCC). The proposed architecture is an optimal controller that augments the conventional bidirectional control of the HESS and serves as a supervisor to ensure optimal dispatch of HESS for inertial support. The architecture is tested on a modified IEEE 123 bus power distribution system, where three dc-microgrids are integrated at different buses using three-phase *d–q* voltage source inverters. Power-sharing determined by the minimization routine is based on the relative angle sensitivity at PCC. Unlike, frequency-droop approach the proposed architecture shares power depending on the proximity of fault/dynamics location from the microgrid of interest. Both inertial and secondary frequency responses are supported by individual dc-microgrids by locally detected ($\Delta\delta$) deviations and the demonstration shows that the architecture shows an improvement of more than 20% in comparison to the conventional frequency-droop method.**

***Index Terms*—Microgrids, grid stability, hybrid energy storage systems (HESSs), three-phase inverter, grid inertia.**

I. Introduction

DUE to the threat posed by climate change and global warming, renewable energy resources such as wind and photovoltaic (PV) are becoming popular choices where additional energy capacity is required to be installed to fulfill load demand. Renewable sources are characterized by low emissions and abundance. However, the intermittent behavior of these sources introduces major operational challenges concerning grid resilience, flexibility, and power quality. To make renewable sources dispatch-able, energy storage sources (ESSs) are introduced and operated in conjunction with them [1]. ESS together with distributed energy resources (DERs) can be implemented anywhere in the grid and provide grid support functionalities such as grid ancillary services and peak load shaving [2], [3]. A range of other grid support services includes black start, energy arbitrage, voltage and frequency regulation, harmonic mitigation, nonspinning reserve, etc. [4]–[7]. To fulfill these functionalities the selection of energy storage must be carried out based on characteristics such as power and energy density, discharge time, response time, life, and cycle time [8]–[11].

The flywheel energy storage system (FESS) is suitable for high power density applications such as system stability enhancements, and grid ancillary service. Numerous articles have demonstrated control of FESS with wind turbine in grid-connected mode [12], [13]. The challenge is the complexity of implementing FESS with all the moving parts and potential space and cost constraints associated with flywheels. The compressed air energy storage system (CAES) works very effectively for both up and down-regulation [14]. However, energy market factors of capacity sizing and investment cost involved are counterproductive for CAES acquisition. The fuel cell is a reliable ESS for microgrid applications. Vidyanandan and Senroy [15] discussed frequency regulation using a hybrid system with a diesel generator, whereas as [16] advantages of fuel cells. However, there are numerous drawbacks such as high cost, reliability, high inflammability, and issues with hydrogen storage.

The Hybrid energy storage system (HESS) is a combination of energy storage devices that enhances the operational capabilities of an individual storage device by providing both high power and energy density. HESS can, thus, be used for applications such as frequency regulation. The frequency regulation curve during grid support operation can be classified into two sections: Primary frequency response (or inertial response) requiring high power density supply and Secondary frequency response (or

Manuscript received November 14, 2020; revised March 31, 2021; accepted May 10, 2021. Date of publication June 16, 2021; date of current version September 16, 2021. Paper 2020-PSEC-1458.R1, presented at the 2020 IEEE International Conference on Power Electronics, Smart Grid and Renewable Energy, Cochin, India, Jan. 2–4, and approved for publication in the IEEE TRANSACTIONS ON INDUSTRY APPLICATIONS by the Power Systems Engineering Committee of the IEEE Industry Applications Society. This work was supported in part by the Electrical and Computer Engineering Department at UNC Charlotte and in part by the National Science Foundation Award ECS-1810174. *(Corresponding author: Sukumar Kamalasadan.)*

The authors are with the Power, Energy and Intelligent Systems Laboratory, Energy Production Infrastructure Center and Department of Electrical Engineering, University of North Carolina at Charlotte, Charlotte, NC 28223 USA (e-mail: ajoshi25@uncc.edu; asuresh4@uncc.edu; skamalas@uncc.edu).

Color versions of one or more figures in this article are available at https://doi.org/10.1109/TIA.2021.3089559.

Digital Object Identifier 10.1109/TIA.2021.3089559

droop response) requiring high energy density supply. The high power density supply for inertial response generally lasts for 5–20 s whereas the secondary response lasts between 30 s and 30 min. A combination of high power density ultracapacitor (UC) and high energy density battery device is an ideal HESS combination to serve this purpose [17]–[21].

For microgrids, dc-link topology is found to be more favorable from power-sharing flexibility and DER integration viewpoint [22]. It is a viable option especially when DER comprises a lot of dc sources and loads. A single inverter sufficiently integrates the entire bus to the larger grid. Studies performed with frequency regulation using DER involve a wide range of frequency-droop variants and optimization to enhance the droop action. For example, authors of [23] have a coordinated control strategy on a wind farm using energy stored in the dc capacitor for a single machine infinite bus system. Virtual inertia is emulated by rotor-side converter capacitance. In another work, similar inertia emulation on the dc-link capacitor for a PV farm and HESS islanded microgrid is illustrated in [24]. Whereas, in [25], virtual inertia emulation of DFIG setup commits maximum power point tracking (MPPT) reserve capacity for frequency regulation. An improved particle swarm optimization algorithm proposed in [26] optimizes the parameters of coupling compensation and inertia for $P-\omega$ and $Q-V$ droop approach even though approximated mathematical models for microgrid are used in these works. In [27], a decoupled frequency and voltage control approach is proposed, which augments the conventional frequency-droop control for power-sharing in a stand-alone microgrid. The battery energy storage system (BESS) can also be used for providing frequency damping capability and improve inertia support from PV farms along with state-of-charge (SOC) management cost function [28]. Electrical coupling of dc-link voltage and ac frequency is discussed in [29] and [30] as unified droop control where ESS supplies for dynamics on both dc link and dc link for a dc–ac microgrid. In this article, we propose an approach that supports both inertia and secondary frequency without requiring knowledge of the system frequency-droop characteristics. The approach has the following advantages in comparison to the state-of-the-art frequency-droop method.

1) Power-sharing for frequency support can be achieved without requiring the knowledge of microgrid droop characteristics.
2) Supports inertial and secondary frequency using locally detected voltage angle deviations.
3) Proposed approach exhibits improved secondary frequency response in terms of settling time when compared with the conventional droop approach.
4) Proposed approach inherently and optimally shares power among multiple DERs.
5) The architecture performs well during changing grid dynamics and is sensitive to the proximity of fault location.
6) Proposed architecture adopts dc-link topology and, hence, favorable for implementation in dc–ac hybrid systems.

In our earlier work, we proposed a PCC angle-based frequency regulation approach using a photovoltaic distributed energy resource consisting of HESS [31]. The novel contributions and the main improvements of this approach, when compared to [31], are as follows.

1) The proposed work uses the rate-of-change of PCC voltage angle as a measure of sensitivity for power management based on the proximity of PCC to the grid.
2) The approach using a multiple dc microgrid and a coordinated control architecture as opposed to one microgrid and PI controller to support that microgrid.
3) The settling time for the proposed architecture improved the settling time by 25–30 s compared to conventional droop and PI-based control.
4) An extensive case study involving real-life LLG and LLLG fault conditions is tested at various locations on the IEEE 123 bus system.

This article is organized as follows. Section III gives a general overview of the proposed architecture. The design of the proposed dc microgrid is detailed in Section II. Section III-A deals with the control of the proposed dc microgrid. The real-time application and scalability of the proposed architecture are validated in Section VI using a modified 123 bus network in the OPAL-RT environment. Section VII concludes this article with a discussion and summary of the proposed approach.

TABLE I
PV MODEL: PARAMETERS AND SPECIFICATIONS

Parameter	Value	Unit
Rated PV farm power	2	MW
Module Open Circuit Voltage	64.2	V
Module Vmpp	54.7	V
Module Short Circuit Current	5.96	A
Module Impp	5.58	A
Series Connected Modules	11	per string
Number of Parallel Strings	596	strings

II. DESIGN OF PROPOSED DC MICROGRID

The design and modeling details of the energy sources in the proposed microgrid which include a 2 MW PV farm, 1.2 MWh lithium-ion battery bank, and an 800 kW, 16 Mega Joules (MJ) UC, are explained as follows.

A. PV Farm Design

For the PV farm, the model of SunPower SPR-205NE-WHT-D, a 305 W PV module is used. Eleven series and 596 parallel combinations of such PV modules result in 600 V, 3.33 kA, 2MW is the PV farm. Temperature and Irradiation profiles can be given as input to the PV farm to simulate related dynamics based on real measurements. For this article, we only consider variations in irradiance and assume temperature to be a standard 25 °C. PV module parameters used for this article are discussed in Table I. For device-level controller design equivalent electrical circuit diagram for a PV cell is modeled as a controlled current source.

TABLE II
BATTERY DISCHARGE CHARACTERISTICS

Parameter	Value	Unit
Maximum Capacity	2000	Ah
Cut-off Voltage	450	V
Fully Charged Voltage	698.39	V
Internal resistance	0.003	Ohms
Capacity at Nominal Voltage	1808.69	Ah

B. Battery Storage System Design

The battery system used in this article is a 1.2 kWh battery of lithium-ion battery, configured for a nominal pack voltage of 600 V and 1200 Ah rated capacity. The initial SOC is specified at 90%. The battery system is designed to be 60% of the PV farm size. The battery discharge characteristics are determined from the nominal voltage and current parameters and shown in Table II.

C. UC Storage System design

An electric double layered capacitor is used as UC storage and modeled in MATLAB/Simulink. The parameters are specified to define Stern model of UC. In this article, the UC is designed for 800 kW peak instantaneous power for up to 20 s. UC bank is designed to 600 V of terminal voltage. The capacitor cell selected has 12 mΩ and operates at 25 °C temperature. A total of 223 such capacitors are arranged in series to obtain a bank rating 600 V at a total capacitance of 95 F. The energy calculation for UC amounts to 16 MJ. The control voltage source E_{uc} is derived using Stern model.

III. PROPOSED ARCHITECTURE

Fig. 1 shows the overall architecture of the proposed microgrid with PV farm and ESSs. The power from the PV farm is managed by a unidirectional dc–dc boost converter operating in input voltage control mode. This allows the PV farm to operate at maximum power point (MPP) and extract an efficient amount of power for the available irradiance. The boost converter also steps-up the output side voltage to near 1200 V which is the dc bus. Since the microgrid is realized in dc-link topology, we have four power converters connecting to the dc bus, namely, the PV converter discussed earlier, two bidirectional dc–dc converters (BDC), and a three-phase $d-q$ grid-connected voltage source inverter (GCVSI). The BDCs are used to regulate the power flowing from HESS into the dc bus based on the outer-loop grid frequency regulation. One of the advantages of operating HESS in a fully active configuration is that each source can be independently controlled and operated at optimal set-points that avoid converter throttling due to maxing of converter ramp-rate. The purpose of selecting 1200 V as dc bus rating is to enable connection of three-phase inverter at the interfacing end. Also, the current flowing through a higher rated dc bus is lower and this contributes to a smaller size of cables and losses. Application-dependent voltage levels of local loads can also be supported by using step-down dc–dc buck converters. Three-phase GCVSI regulates the dc-bus voltage at the rated 1200 V.

A. Primary Level Control of Proposed DC Microgrid

The proposed inner-loop control architecture of the dc microgrid is shown in Fig. 1. It consists of a three-phase $d-q$ inverter primary level control and an HESS secondary level control. The control on PV farm is directed towards the successful extraction of MPP power.

1) Control of Nondispatchable Source: PV Farm: A PV farm is a current source and to maximize its output we use MPP as a reference. To achieve this we need to drive the PV plant at the Voltage (V_{MPP}) corresponding MPP using an input voltage controlled dc–dc converter. A dc–dc converter comprises of two filter elements and, hence, is defined as a second order system. Based on the volt − second and capacitor − charge balance equations for the converter the state space representation is given as

$$\begin{bmatrix} \dot{\overline{i_{pv}}} \\ \dot{\overline{V_o}} \end{bmatrix} = \begin{bmatrix} 0 & \frac{-d'_{pv}}{L} \\ \frac{d'_{pv}}{C} & \frac{-1}{RC} \end{bmatrix} \begin{bmatrix} \overline{i_{pv}} \\ \overline{V_o} \end{bmatrix} + \begin{bmatrix} \frac{1}{L} & 0 & \frac{V_o}{L} \\ 0 & \frac{-1}{C} & \frac{i_{pv}}{C} \end{bmatrix} \begin{bmatrix} \overline{V_{pv}} \\ \overline{i_o} \\ \overline{d_{pv}} \end{bmatrix} \quad (1)$$

$$\begin{bmatrix} V_o \\ i_{pv} \end{bmatrix} = \begin{bmatrix} 0 & 1 \\ 1 & 0 \end{bmatrix} \begin{bmatrix} \overline{i_{pv}} \\ \overline{V_o} \end{bmatrix} \quad (2)$$

where $\overline{V_{pv}}$ is the input side voltage, $\overline{i_o}$ is the output side current, and $\overline{d_{pv}}$ is the duty cycle input to the converter for boost operation, $\overline{i_{pv}}$, $\overline{V_{pv}}$, and $\overline{V_o}$ are inductor current, input voltage, and output voltage, respectively, and the states of the converter. L, C, and d'_{pv} are the inductor, capacitor, and the duty cycle for buck operation of the converter.

The control-to-input voltage transfer function for dc–dc boost converter of the PV farm can be derived as

$$\frac{\overline{V_{pv}}(s)}{\overline{d_{pv}}(s)} = \frac{(1-d_{pv})^2 V_o - (1-d_{pv}) L I_l s}{(LC)s^2 + (\frac{L}{R})s + (1-d_{pv})^2} \quad (3)$$

where V_{pv} is the small signal Input voltage, d_{pv} is the small signal duty cycle, L, C are the dc–dc converter design elements and R is the load resistance. PV control diagram from the perspective of overall architecture on dc microgrid is shown in Fig. 1. Considering an uncompensated bode plot it was observed that the system has phase margin (PM) of $-89.8°$ and a negative gain margin (GM) of -55.6 dB. To exercise control a PI compensation given by (4) is derived. The PI controller transfer function is given as

$$G_c(s) = -1.5 - \frac{7}{s}. \quad (4)$$

If we write (3) transfer function as a gain $G_{pv}(s)$, the closed-loop PV boost converter along with the PI control can be given as

$$G_{clpv}(s) = \frac{G_{cpv}(s) G_{pv}(s)}{1 + G_{cpv}(s) G_{pv}(s)} \quad (5)$$

$$G_{clpv}(s) = \frac{7s^2 - 422s - 1800}{0.0001215s^3 + 7.008s^2 - 421.7s - 1800} \quad (6)$$

where $G_{clpv}(s)$ is the closed-loop gain of the compensated system, $G_{cpv}(s)$ is the controller gain in the forward path, $G_{pv}(s)$

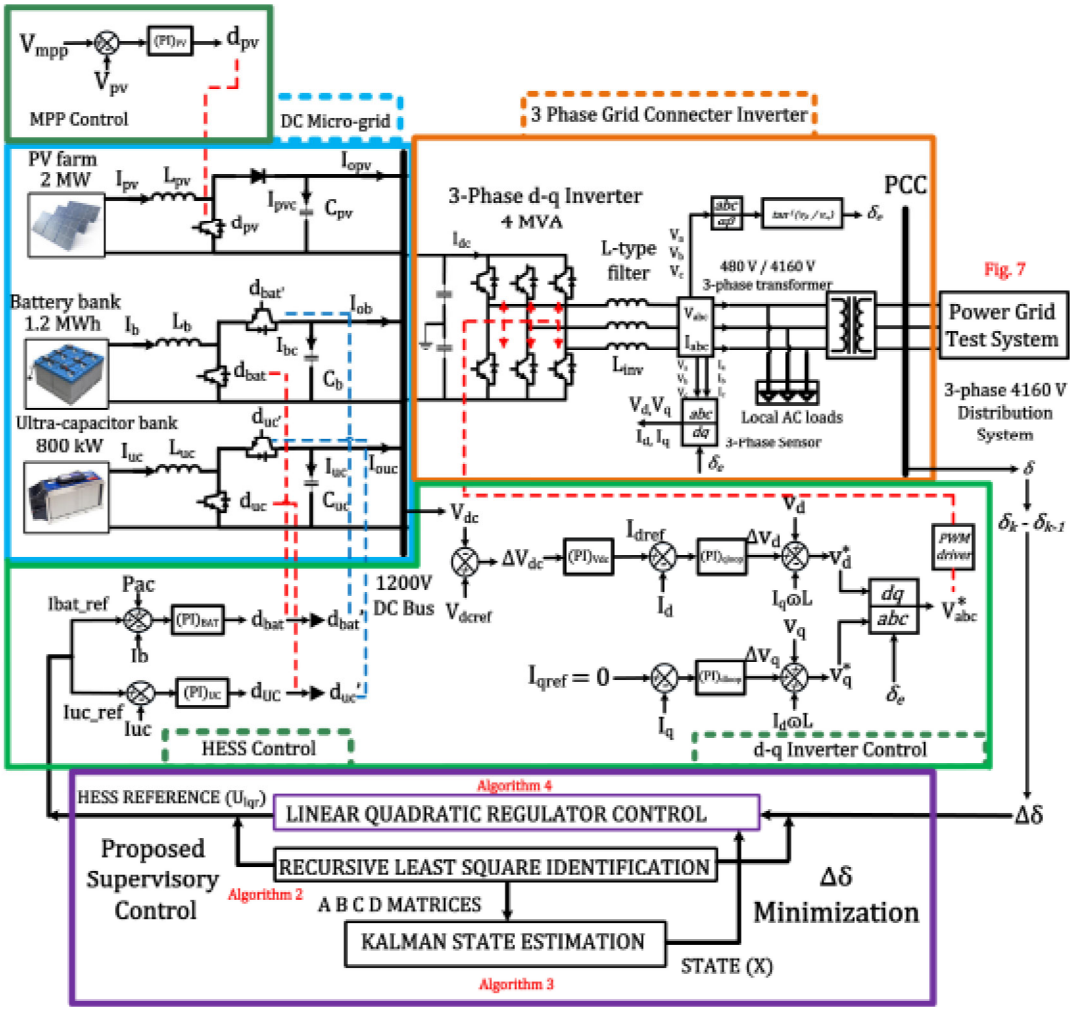

Fig. 1. Proposed dc microgrid.

is the plant gain represented by transfer function given in (3). The step response showed acceptable characteristics.

2) Primary Level of Control—Inverter: The objective of the primary level of control is to regulate the dc bus to its rated 1200 V set point. This is realized with the implementation of a three-phase GCVSI with a power rating of 4 MVA at the point of common coupling (PCC). The size of the inverter is calculated based on the maximum power rating of dc devices in the microgrid such that the inverter is capable of sending through all the available dc power in the event of total dc discharge. The inverter is operated based on a $d-q$ control. Inverter angle (δ_e) and frequency information are obtained using phase-locked loop (PLL) at the grid-connected mode. The output of PLL (δ_e) is used to synchronize the abc to $d-q$ transformation and is shown in Fig. 1. The voltage balance equations for an L-type inverter can be written in state-space form and d–q framework as

$$\begin{bmatrix} \dot{i}_d \\ \dot{i}_q \end{bmatrix} = \begin{bmatrix} 0 & \omega \\ -\omega & 0 \end{bmatrix} \begin{bmatrix} i_d \\ i_q \end{bmatrix} + \begin{bmatrix} \frac{1}{L_{\text{inv}}} & 0 \\ 0 & \frac{1}{L_{\text{inv}}} \end{bmatrix} \begin{bmatrix} (V_{dl} - V_d) \\ (V_{ql} - V_q) \end{bmatrix} \quad (7)$$

where V_{dl} and V_{ql} are d-axis and q-axis voltages across inductor L_{inv}, ω is the angular frequency of the supply voltage, L is the inductance of the L-type filter, i_d, i_q and V_d, V_q are the d-axis and q-axis inverter output current and voltages, respectively [32]. Active and reactive power output of the grid-connected inverter (GCI) can be given in d–q domain as

$$\begin{bmatrix} P_{\text{inv}} \\ Q_{\text{inv}} \end{bmatrix} = \begin{bmatrix} V_d & V_q \\ V_q & -V_d \end{bmatrix} \begin{bmatrix} i_d \\ i_q \end{bmatrix}. \quad (8)$$

During steady-state grid operation, we can consider voltage magnitude of grid, V_d, to be a constant. Thus, the active and reactive power of the GCVSI can be controlled by controlling i_d and i_q. The transfer function of d-axis current ($\overline{i_d}$) versus ($\overline{\Delta V_d}$) can be given in Laplace domain as

$$\frac{\overline{i_d}(s)}{\overline{\Delta V_d}(s)} = \frac{s}{L_{\text{inv}} V_d} \left(\frac{V_d + V_q}{s^2 + \omega^2} \right) \quad (9)$$

where ΔV_d is $V_{dl} - V_d$, s is the Laplace operator. For the specific design, the inverter transfer function can be derived as

$$G_{\text{inv}}(s) = \frac{\overline{i_d}(s)}{\overline{\Delta V_d}(s)} = \frac{s}{s^2 + 1}. \quad (10)$$

For the inner-loop PI controller design, first the transfer function is converted into discrete (z) domain using a zero-order hold for a simulation time step of 400 μs. Then, the system parameters are per unitized on the base of rated values. The per unitized transfer function shown in (10) is used for PI tuning to get satisfactory step response. The obtained values are K_p and K_i values of 0.86 and 0.6, respectively. The equivalent PI controller is designed as

$$G_{\text{cinv}}(s) = 0.86 + \frac{0.6}{s}. \tag{11}$$

The closed-loop transfer function will then be

$$G_{\text{clinv}}(s) = \frac{0.86s + 0.6}{s^2 + 0.86s + 1.6} \tag{12}$$

where $G_{\text{clinv}}(s)$ is the closed-loop gain of the compensated inverter system, $G_{\text{cinv}}(s)$ is the inverter controller gain in the forward path, $G_{\text{inv}}(s)$ is the inverter transfer function.

For the outer loop, (14) is used. Fig. 1 showcases the d–q control structure applied on the inverter to exercise control on the active and reactive power of GCI.

3) Primary Level of Control—HESS: The HESS is modeled in a fully active configuration with separate bidirectional converters for each of its components [33]. The HESS is connected in a dc-link topology along with the PV farm through dc–dc converters at 1200 V dc bus. The battery is designed for a 900 kW, 1.2 MWh rating, which is 60% of the PV size, whereas the UC is designed for 800 kW peak instantaneous power for up to 20 s. The primary level controller design is based on the state-space modeling of the dc–dc converter represented as

$$\begin{bmatrix} \dot{\bar{i}} \\ \dot{V}_{\text{dc}} \end{bmatrix} = \begin{bmatrix} 0 & \frac{-d'_{\text{bat}}}{L} \\ \frac{d'_{\text{bat}}}{C} & \frac{-1}{RC} \end{bmatrix} \begin{bmatrix} \bar{i} \\ \overline{V_{\text{dc}}} \end{bmatrix} + \begin{bmatrix} \frac{1}{L} & 0 & \frac{V}{L} \\ 0 & \frac{-1}{C} & \frac{i}{C} \end{bmatrix} \begin{bmatrix} \overline{V_{\text{bat}}} \\ \overline{i_{\text{dc}}} \\ \overline{d_{\text{bat}}} \end{bmatrix} \tag{13}$$

$$\begin{bmatrix} V_{\text{dc}} \\ i \end{bmatrix} = \begin{bmatrix} 0 & 1 \\ 1 & 0 \end{bmatrix} \begin{bmatrix} \bar{i} \\ \overline{V_{\text{dc}}} \end{bmatrix} \tag{14}$$

where $\overline{V_{\text{bat}}}$ is the input side voltage, $\overline{i_{\text{dc}}}$ is the output side current, and $\overline{d_{\text{bat}}}$ is the duty cycle input to the converter for boost operation, $\bar{i}$, $\overline{V_{\text{bat}}}$, and $\overline{V}$ are inductor current, input voltage, and output voltage, respectively, and the states of the converter. L, C, and d'_{bat} are the inductor, capacitor, and the duty cycle for buck operation of the converter. From the mentioned above, we can obtain the transfer function of control-to-input side current as

$$\frac{\bar{i}(s)}{\overline{d_{\text{bat}}}(s)} = \frac{s\frac{V}{L} + \frac{V}{RLC} + \frac{id'_{\text{bat}}}{C^2}}{s^2 + \frac{s}{RC} + \frac{d'^2_{\text{bat}}}{LC}} \tag{15}$$

where $\bar{i}(s)$ is I_b and $\overline{d_{\text{bat}}}(s)$ is d_{bat} from Fig. 1. The per unit transfer function of (15) can be represented as

$$G_{\text{bat}}(s) = \frac{\bar{i}(s)}{\overline{d_{\text{bat}}}(s)} = \frac{s + 1.5}{s^2 + s + 0.25}. \tag{16}$$

It was found that the abovementioned system has an infinite GM and 82.8° PM. The system is stable by default but the step response settles to 0.856 per unit. Based on this the PI controller is designed as

$$G_{\text{cbat}}(s) = 1.3 + \frac{3}{s}. \tag{17}$$

The closed-loop dc–dc converter plant along with the PI control can be given as

$$G_{\text{clbat}}(s) = \frac{1.3s^2 + 4.95s + 4.5}{4.3s^2 + 7.95s + 5.25} \tag{18}$$

where $G_{\text{clbat}}(s)$ is the closed-loop gain of the compensated battery converter system, $G_{\text{cbat}}(s)$ is the controller gain, and $G_{\text{bat}}(s)$ is the battery converter transfer function.

The control design is summarized in the Table III.

TABLE III
CONTROLLER GAINS AFTER DESIGN AND TUNING

Control Loop	k_p	k_i
HESS Current/Power	1.3	3
Inverter d-axis current/Active Power	0.86	0.6
Inverter q-axis current/Reactive Power	-0.86	-0.6
PV MPPT	-1.5	-7
Inverter DC link regulation	-0.9	-3

IV. PROPOSED SUPERVISORY CONTROL

The supervisory controller in this work is designed such that the HESS delivers additional power to maintain frequency imbalances of the grid by monitoring the changes in the voltage angle ($\Delta\delta$). During power grid dynamics, frequency deviations are observed in the electrical network. In this architecture HESS and the inverter coordinate to provide additional active power to maintain the frequency. Generally, such controllers are designed through frequency-droop known as frequency regulation for both primary and secondary level responses. However, the droop approach requires considerable knowledge of microgrid capacity and dynamics. Such a control loop heavily depends upon the appropriateness of the droop constant and they are static (gains cannot be changed with system dynamics). The proposed approach utilizes error minimization on inverter voltage angle deviations, which in turn help regulate frequency. To arrive at the open-loop transfer function, we will first discuss a couple of assumptions regarding efficiencies of the power converters used in the microgrid, namely BDCs and three-phase d–q inverter. Considering BDC's are lossless dc power can be written as

$$P_{\text{dc}} = P_b + P_{\text{uc}}, P_{\text{inv}} = P_{\text{dc}}, V_{\text{dc}}I_{\text{dc}} = V_bI_b + V_{\text{uc}}I_{\text{uc}} \tag{19}$$

where P_{dc} is the total power output from BDCs at dc bus, P_b is the power input to battery BDC, P_{uc} is the power input to UC BDC, P_{inv} is the active power at the inverter output, V_{dc} is the dc-bus voltage, I_{dc} is the dc-bus current, V_b is the input-side converter voltage across battery source (battery terminal voltage), V_{uc} is the input-side converter voltage across UC source (UC terminal voltage), I_b is the input-side converter current from battery source (battery terminal current), and I_{uc} is the input-side converter current from UC source (UC terminal current). The power transfer through an inductive line, assuming $\sin(\delta) \approx \delta$

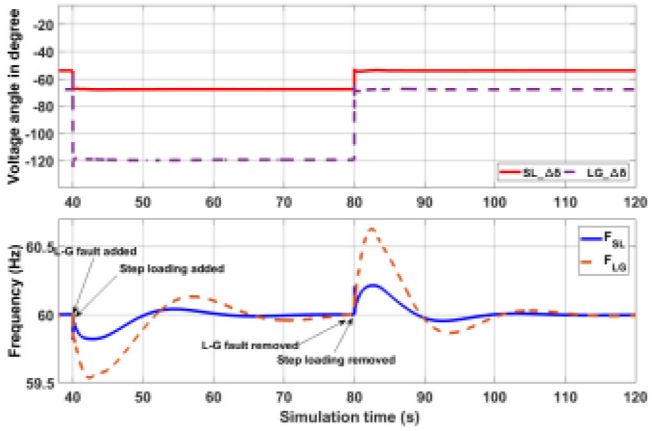

Fig. 2. Voltage angle response to grid dynamics on modified 123 bus system.

can be written as

$$P_{\text{inv}} = \frac{V_1 V_2 \delta}{X} \tag{20}$$

where P_{inv} is the three-phase ac active power, V_1 is the sending end voltage, V_2 is the receiving end voltage, δ is the voltage angle difference between V_1 and V_2 and X is the inductive reactance between the sending and receiving end. The state-space representation of the dc–dc boost converter discussed in Section II-A gives us the relationship between output-side voltage and input-side current as

$$\frac{V_{\text{dc}}(s)}{I_{\text{bat}}(s)} = \frac{s\frac{I_{\text{lin}}}{C} - \frac{V_{\text{dc}}D'}{L}}{s\frac{V_{\text{dc}}}{L} + \frac{V_{\text{dc}}}{RLC} + \frac{I_{\text{lin}}D'}{C^2}}. \tag{21}$$

Using (19)–(21), we get

$$\frac{\Delta\delta(s)}{I\text{bat}_{\text{ref}}(s)} = \frac{s\frac{X I_{\text{dc}} I_{\text{lin}}}{C} + \frac{P_{\text{dc}} X D'}{L}}{s\frac{V_{\text{dc}} V_1 V_2}{L} + \frac{V_{\text{dc}} V_1 V_2}{RLC} + \frac{I_{\text{lin}} D' V_1 V_2}{C^2}} \tag{22}$$

where $I\text{bat}_{\text{ref}}$ is battery current reference and $\Delta\delta$ is PCC angle deviation represented in Fig. 1.

From the abovementioned, an eighth-order aggregated closed-loop transfer function is derived, which can then be represented as

$$\frac{y(k)}{u(k)} = \frac{\Delta\delta(k)}{I\text{bat}_{\text{ref}}(k)} = C_{ss}(zI - A_{ss})^{-1}B_{ss} \tag{23}$$

where C_{ss} is the output matrix, z is the discrete domain operator, I is the eighth-order identity matrix, A_{ss} is the state transition matrix, and B_{ss} is the Input matrix of the closed-loop state-space representation.

A. Behavior of Voltage Angles During Dynamics

To understand how voltage angle at the PCC changes during grid dynamics we simulate step-loading and line-to-ground (L–G) fault conditions on a modified IEEE 123 bus system. From Fig. 2, it can be observed that the angle (δ) at PCC decreases with increased loading on the system. Simultaneously, the grid frequency also drops. This implies that the primary and secondary response of frequency can be controlled by minimizing the rate of change of angle ($\Delta\delta$) during grid dynamics by providing power from the microgrid. Algorithm 1 provides overall integration methodology.

Algorithm 1 Frequency Based LQR Output Reset.

Step: 1 Collect PCC voltage angles $\delta(k)$ and $\delta(k-1)$ for current and previous time step
Step: 2 Collect grid frequency measurement at PCC, f
Step: 3 Collect Control output, U_{lqr}
if $\delta(k) \neq \delta(k-1)$ *and* $59.995 \geq f \geq 60.005$ **then**
  $U_{lqr} = U_{lqr}$
else
  Apply 20% down the ramp on controller output,
  $U_{lqr} = U_{lqr}$ - $0.2U_{lqr}$

From the abovementioned, it can be seen that the supervisory loop is dormant when there is no change in angle. The reset operation on the integrator is also a trigger dependent on whether grid frequency is close to regulation. To achieve an optimal solution for energy storage set point with a view of minimizing the rate of change of δ, an optimal controller evolved from the linear–quadratic regulator (LQR) is designed.

B. Optimal Supervisory Controller Design

Optimal controller design consists of identifying the discrete form of the transfer function in (30) using a measurement-based identifier and then developing a state-space representation of the power grid dynamics.

1) Grid Identification: Equation (24) is a generalized form of the eighth-order transfer function relationship that is identified by the recursive least square identification

$$\frac{y(k)}{u(k)} = \frac{b_1 z^{-1} + b_2 z^{-2} + \cdots + b_n z^{-n}}{1 + a_1 z^{-1} + a_2 z^{-2} + \cdots + a_n z^{-n}} \tag{24}$$

where as and bs are the denominator and numerator coefficients of the transfer function, respectively. The numerator and denominator polynomials in terms of as and bs from (24) are used to generate the A, B, and C matrices (23) that constitute the closed-loop microgrid state space.

Important parameters regarding the identification process that need to be chosen are the order of the system (n) to be identified and the length of the observable window (N) for which inputs and outputs need to be populated and held

$$N = 2 \cdot n \tag{25}$$

where N is the length of the observable window in terms of the number of samples and n is the order of the system.

To estimate the transfer function of $\Delta\delta(k)$ with respect to LQR output $I\text{bat}_{\text{ref}}(k)$, we need to include the dynamics of BDCs and the three-phase inverter. One BDC can be captured using a second-order system whereas a three-phase inverter is a second-order system. Since we have individual BDCs for each energy storage device in our HESS, an eighth-order identification process should not only suffice but also be successful in

Algorithm 2: Recursive Least Square Identification.

Step: 1 Populate matrix $X_{ls}[N \times 2n]$ with past inputs ($Ibat_{ref}$) and outputs ($\Delta\delta$) for the observable sample window

Step: 2 Select the latest ($Ibat_{ref}$) and ($\Delta\delta$) samples for processing in matrix $x_{ls}[1 \times 2n]$.

Step: 3 Populate Φ as matrix with output samples ($\Delta\delta$)

Step: 4 Initialize Matrices P_{ls}, K_{ls} and Θ and constant γ.

Step: 5 Calculate

$$P_{ls}(k) = \frac{[I - K_{ls}(k)x'_{ls}(k)]\, P_{ls}(k-1)}{\gamma}$$

Step: 6 Calculate

$$K_{ls}(k) = \frac{P_{ls}(k-1)x_{ls}(k)}{\gamma + x'_{ls}(k)P_{ls}(k-1)x_{ls}(k)}$$

Step: 7 Update

$$\Theta(k) = \Theta(k-1) + K_{ls}(k)\,[\Phi(k) - x'_{ls}(k)\Theta(k-1)]$$

Algorithm 3: Kalman State Estimation.

Step: 1 Initialize Matrices $\hat{X_{ke}}$, P_{ke}, Q_{ke}, K_{ke}, R_{ke}, Res

Step: 2 Collect ($Ibat_{ref}$) and ($\Delta\delta$) samples and arrange in Matrices U and y respectively, include the RLS identified state space matrices A_{ss}, B_{ss}, C_{ss}

Step: 3 Calculate the initial estimate of states $\hat{X_{ke}}$

$$\hat{X_{ke}}(k) = A_{ss}(k) \cdot \hat{X_{ke}}(k-1) + B_{ss}(k) \cdot U(k)$$

Step: 4 Calculate the Error Co-variance Estimate

$$P_{ke}(k) = A_{ss}(k) \cdot P_{ke}(k-1) \cdot A^T_{ss}(k) + Q_{ke}$$

Step: 5 Calculate the Kalman Gain:

$$K_{ke}(k) = \frac{P_{ke}(k) \cdot C^T_{ss}(k)}{C_{ss}(k) \cdot P_{ke}(k) \cdot C^T_{ss}(k) + R_{ke}}$$

Step: 6 Calculate the measurement residue

$$Res(k) = y(k) - C_{ss}(k) * \hat{X_{ke}}(k)$$

Step: 7 Update the Error Co-variance Estimate

$$P_{ke}(k) = [I - K_{ke}(k) \cdot C_{ss}(k)] \cdot P_{ke}(k)$$

Step: 8 Update the State Co-variance Estimate

$$\hat{X_{ke}}(k) = \hat{X_{ke}}(k) + K_{ke}(k) \cdot Res(k)$$

capturing unknown system dynamics for the test system under study. The algorithm is as follows.

2) Grid State estimation: Grid state estimation develops the state information based on the grid identification. For an eighth-order identification, grid state estimation provides eight states. This is performed based on Kalman state estimation algorithm. The details of Kalman-based state estimation are illustrated in algorithm 3.

3) Optimal Controller: In the proposed optimal control:

The discrete LQR formulation specific to our control problem is shown as follows:

$$J = \sum_{0}^{\infty} (\Delta\delta^T(k) \cdot Q(k) \cdot \Delta\delta(k) + I\text{bat}^T_{\text{ref}}(k) \cdot R \cdot I\text{bat}_{\text{ref}}(k)) \quad (26)$$

$$Q(k) = 20 * C'(k) \cdot C(k) \quad (27)$$

where J, is the linear–quadratic function, $\Delta\delta^T(k)$ is the transpose of the dynamically changing state of interest, Q is the static penalty factor associated with the state, $I\text{bat}^T_{\text{ref}}(k)$ is the transpose of the recursively generated optimal control and input to the plant in a closed loop, $R = 0.1$ is the static penalty factor associated with the input, $Q(k)$ is the penalty factor for state. To implement a controller based on such dynamic quadratic optimization, we need to utilize system state space that captures system parameters dynamically. This is provided by a least square-based identification process that recursively estimates and updates the state space of the system.

Algorithm 4: Linear Quadratic Regulator Control.

Step: 1 Extract RLS identified state space matrices A_{ss}, B_{ss}, C_{ss} and Kalman Estimate $\hat{X_{ke}}$

Step: 2 Set $Q_{lqr}(k) = 20 \cdot C^T_{ss}\, C_{ss}$, $R_{lqr} = 0.1$ and initialize Algebraic Riccati Solution $P_{lqr}(k-1)$ and the time period of the LQR call function in simulation, T_c

Step: 3 Solve for Algebraic Riccati Equation

$$P_{lqr}(k) = [P_{lqr}(k-1) \cdot A_{ss}(k) + A^T_{ss}(k) \cdot P_{lqr}(k-1) - P_{lqr}(k-1) \cdot B_{ss}(k) \cdot R^{-1}_{lqr}(k) \cdot B^T_{ss}(k) \cdot P_{lqr}(k-1) + Q_{lqr}(k)] \cdot T_c + P_{lqr}(k-1)$$

Step: 4 Find LQR gain K_{lqr} for k^{th} time

$$K_{lqr}(k) = R^{-1}_{lqr} \cdot B^T_{ss}(k) \cdot P_{lqr}(k)$$

Step: 5 The optimal control output $Ibat_{ref}$ is given by:

$$Ibat_{ref}(k) = -K_{lqr}(k) \cdot \hat{X_{ke}}(k)$$

At the end of Algorithm 2, we get the Θ matrix, which consists of dynamically changing as and bs that form the transfer function, as shown in (24). The state-space deduced using this transfer function is used to run the optimization discussed in Section IV-B obtained from state-space representation where $A_{ss}(k)$, $B_{ss}(k)$, and $C_{ss}(k)$ are the state transition, input, and output matrices, respectively. Algorithm 3 details the step-wise process of estimating the state of interest ($\Delta\delta$) from the RLS identified system. The state estimate from Algorithm 3 is used to calculate the optimal control output of LQR. LQR gain (K_{LQR}) for every sample is calculated using a 2-step process given in Algorithm 4, which gives the optimal control output, $I\text{bat}_{\text{ref}}$.

The summary of the closed-loop multilevel control structure is given by frequency domain loop gain as shown in the following

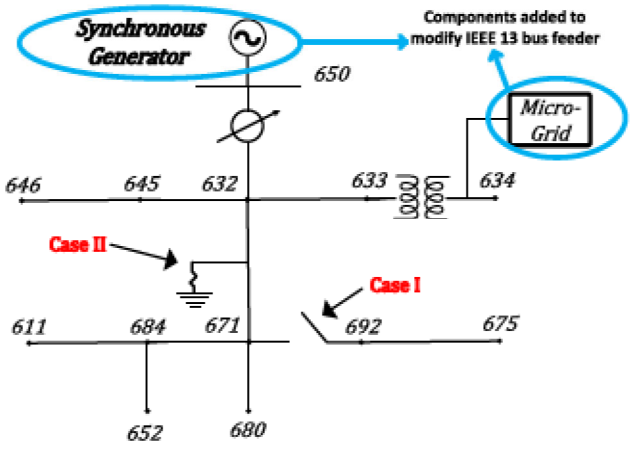

Fig. 3. Modified IEEE 13 bus system with microgrid and synchronous generator model.

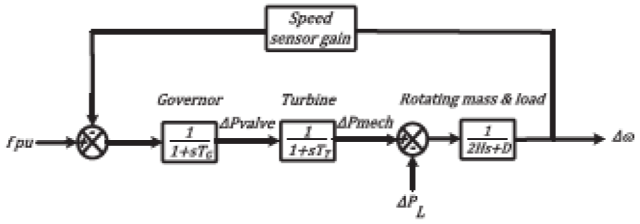

Fig. 4. Speed governor control for synchronous generator.

equation:

$$G(s) = \frac{\Delta\delta(s)}{Ib_{\text{ref}}(s)} * \frac{Ib_{\text{ref}}(s)}{d(s)} * \frac{d(s)}{V\text{dc}(s)} * \frac{V\text{dc}(s)}{i_d^{\text{ref}}(s)} * \frac{i_d^{\text{ref}}(s)}{\Delta V_d(s)} \tag{28}$$

where $\frac{V\text{dc}(s)}{i_d^{\text{ref}}(s)} * \frac{i_d^{\text{ref}}(s)}{\Delta V_d(s)}$ represents the inverter d–q control (primary level), $\frac{Ib_{\text{ref}}(s)}{d(s)}$ is the battery current control applied by BDC in dc microgrid, $\frac{d(s)}{V\text{dc}(s)}$ represents the effect of input side current control on dc-bus voltage and $\frac{\Delta\delta(s)}{Ib_{\text{ref}}(s)}$ describes the gain for the supervisory controller.

V. Proof-of-Concept Study

For the proof-of-concept study, a modified IEEE 13 bus system [34], with the proposed microgrid with control architecture and asynchronous generator model as a source in MATLAB-Simulink environment is designed. The microgrid structure is integrated at bus 634. Fig. 3 shows the modified IEEE 13 bus system and the PCC for microgrid. Bus 634 of the modified test system operates at 480 V, which makes microgrid integration favorable. GCI is designed for a 4 MVA rating and operates at 480 V at its output. Also, a synchronous generator is added with a governor control to emulate the inertial response of the generator to fault or power mismatch as shown in Fig. 4. fault or power mismatch.

Two cases are studied. In Case 1, lines between bus 671 and 692 from Fig. 3 are closed at 100 s simulation time to add 800 kW of three-phase unbalanced loads. The step change in loading on the modified 13 bus system is simulated as a power mismatch. In Case 2, an L–G fault as shown in Fig. 3 at bus 671 is initiated.

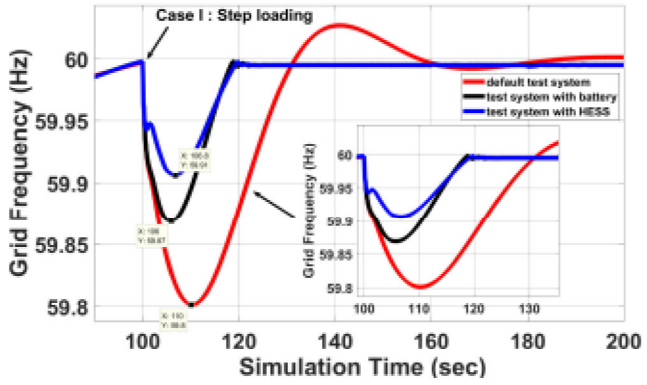

Fig. 5. Case I: Frequency regulation for (800 kW / 10%) LLG @ 100 s.

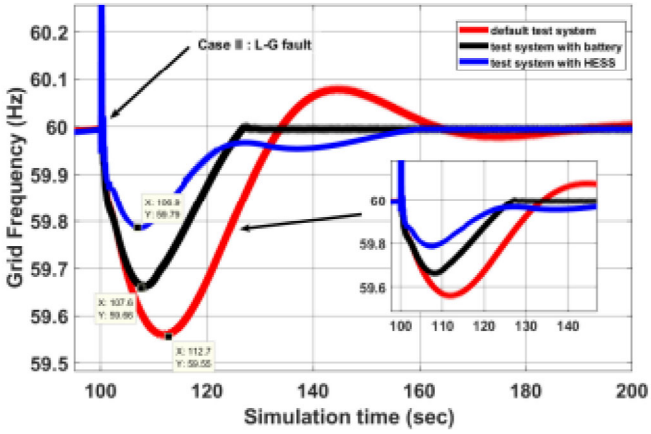

Fig. 6. Case II: Primary and secondary frequency response for the system.

Frequency response to LLG (Case I): In this case, when a 10% step change in load is injected into the system the frequency nadir reaches 59.8 Hz for the modified 13 bus system with synchronous generator. The secondary response took about 166 s to settle. With the proposed microgrid integrated architecture the frequency nadir improves to 59.87 Hz. The secondary response settles at 125 s, a significant improvement compared to the modified 13 bus system. In comparison to this, the HESS system reduces frequency nadir to 59.91 Hz with a settling time similar to BESS. A performance comparison between HESS and BESS indicated that the contribution of UC in reducing the frequency nadir.

Frequency response to L–G Fault (Case II): The severity of the L–G fault on the power grid is evident in Fig. 6, where the frequency nadir is seen dropping as low as 59.55 Hz for the modified 13 bus system. The addition of HESS slightly improves frequency to 59.79 Hz as opposed to 59.66 Hz for the BESS case. The settling time for the modified 13 bus system is around 183 s compared to 160 s after HESS addition. BESS case frequency settles the earliest at about 125 s. Table IV summarizes the case study performed on the modified 13 bus system. The following abbreviations are used during the formulation of the table and also apply to Table V: MBS is modified bus system; Imp Vs MBS is improvement versus modified bus system.

TABLE IV
RESULTS ON MODIFIED 13 BUS NETWORK

	Parameter	MBS	MBS + HESS	Imp Vs MBS
Case I	Nadir (Hz) Settl. time (*s*)	59.8 166	59.91 125	55% 41
Case II	Nadir (Hz) Settl. time (*s*)	59.55 183	59.79 160	53.33% 23

Sample calculations for Table V are discussed as follows:

$$f_1 = \frac{\text{Nominalfrequency} - \text{ProposedApproachFrequency}}{\text{Nominalfrequency}} \tag{29}$$

$$f_1 = \frac{60 - 59.58}{60} = 0.007 \tag{30}$$

$$f_2 = \frac{\text{Nominalfrequency} - \text{MBSFrequency}}{\text{Nominalfrequency}} \tag{31}$$

$$f_2 = \frac{60 - 59.52}{60} = 0.008 \tag{32}$$

$$f_{\text{improvement}} = \frac{0.008 - 0.007}{0.008} = 0.125 = 12.5\%. \tag{33}$$

VI. REAL-TIME ARCHITECTURE VALIDATION ON MODIFIED IEEE 123 BUS NETWORK

The scalability of the proposed structure is tested using an IEEE 123 bus feeder [34]. This test feeder is a medium-size network with multiple load regulators and shunt capacitors. It is characterized by spots, unbalanced loading, and switches to alternate the power-flow path. For this work, a modified IEEE 123 bus system, involving three microgrids and a synchronous generator model is designed in a MATLAB-Simulink environment and simulated in real-time using OPAL-RT, RT-LAB environment. The synchronous generator is added with a governor control as described in Section V at bus 149 and microgrids are integrated at buses 21, 86, and 300. Fig. 7 shows the GB security and quality of supply standard (GB-SQSS) frequency response of power grid to dynamic conditions in terms of ROCOF, primary and secondary frequency regulation. The response can vary from several seconds to a few minutes.

LLG (Case I) and LLLG fault (Case II) events are simulated to study the response of the proposed architecture and the power-sharing it provides for DERs. Subcases for buses 51, 18, and 67 will be defined with alphabetical suffixes A, B, and C, respectively. For each of the subcases, the effect of LLG (Case I) and LLLG fault (Case II) will be observed on ($\Delta\delta$) for every microgrid. Furthermore, the response of the supervisory LQR control will be recorded for each microgrid. Thus, the contribution of microgrids toward frequency regulation can be determined based on the proximity of the fault location. Fig. 8 shows test cases I-A, I-B, I-C, II-A, II-B, and II-C performed on the modified 123 bus system. Fig. 9 illustrate the real-time test-bed.

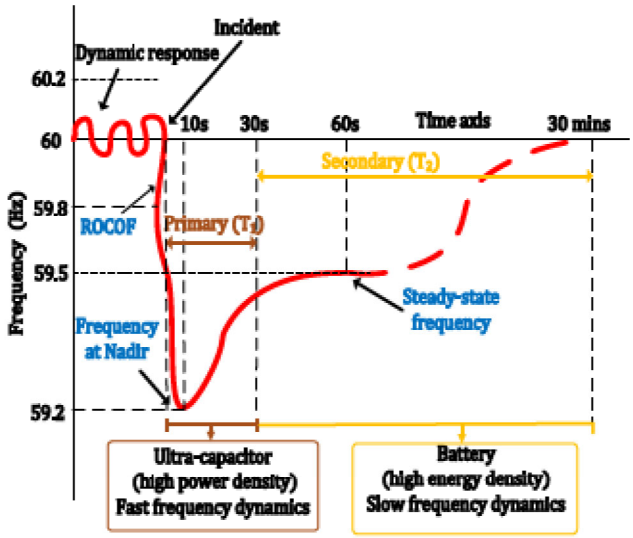

Fig. 7. GB-SQSS frequency response of power grid.

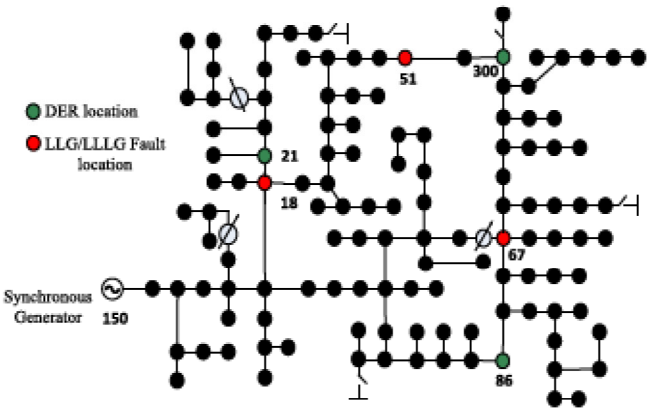

Fig. 8. Microgrid integration study for a 123 bus feeder.

A. Frequency Response to LLG (Case I)

1) Fault Location 51 (Case I-A): Fig. 10 discusses the response of the three microgrids to the LLG fault on bus 51. The fault is created and removed within 0.18 s. The first subplot shows the graphs of the rate of change of $\Delta\delta$ with respect to time on the individual microgrid buses. It can be observed that the $\Delta\delta$ shows the maximum change for bus 300 as a reaction to the LLG fault. This is because bus 300 is closest to the fault location as compared to the other two buses. Thus, the microgrid connected at bus 300 supplies the maximum power of 0.3775 p.u., as shown in Fig. 10. Microgrid at bus 86 is the next closest and supplies a peak power of 0.2524 p.u. on the base of the dispatch-able HESS, which is rated at 1700 kW. Microgrid at bus 21 is the farthest away and contributes 0.2275 p.u. power to frequency regulation. As a result of frequency support from HESS, the frequency nadir improves to 59.58 Hz in comparison to 59.52 Hz for the default system response with the synchronous generator (shown in Fig. 11). The conventional frequency-droop approach performs the best with a frequency nadir of 59.6 Hz. Whereas, the $\Delta\delta$

TABLE V
RESULTS ON MODIFIED 123 BUS NETWORK

Event location	Parameter	MBS	MBS + Proposed Approach	Imp Vs MBS	MBS + Droop Approach	Imp Vs MBS
Case I-A bus 51	Frequency Nadir (Hz)	59.52	59.58	12.5%	59.6	16.66%
	Settling time (s)	66	5.84	60.16	31.88	34.12
Case I-B bus 18	Frequency Nadir (Hz)	59.46	59.54	9.61%	59.55	15.38%
	Settling time (s)	70	6.92	63.08	29	41
Case I-C bus 67	Frequency Nadir (Hz)	59.52	59.58	12.5%	59.6	16.66%
	Settling time (s)	68	5.37	62.63	35	33
Case II-A bus 51	Frequency Nadir (Hz)	59.33	59.48	22.38%	59.46	19.4%
	Settling time (s)	80	8	72	31.91	48.09
Case II-B bus 18	Frequency Nadir (Hz)	59.32	59.48	25%	59.46	19.11%
	Settling time (s)	78	7.16	70.84	32	46
Case II-C bus 67	Frequency Nadir (Hz)	59.32	59.49	25%	59.45	19.11%
	Settling time (s)	76	7.66	68.34	39.42	46.58

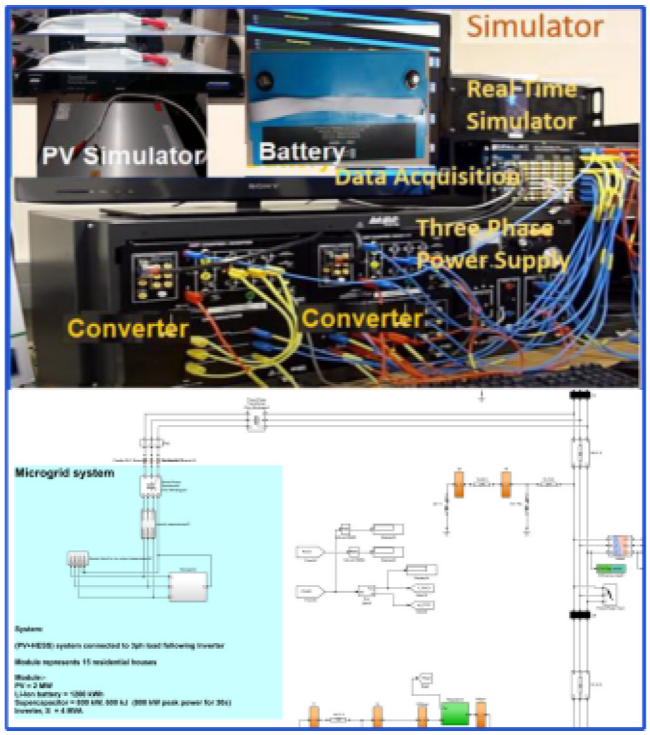

Fig. 9. Real-time experimental test-bed.

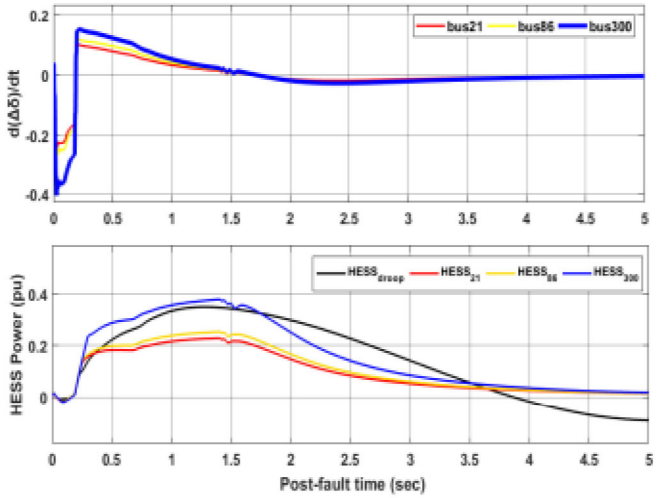

Fig. 10. Case I-A: DER HESS power sharing based on $\Delta\delta$ minimization.

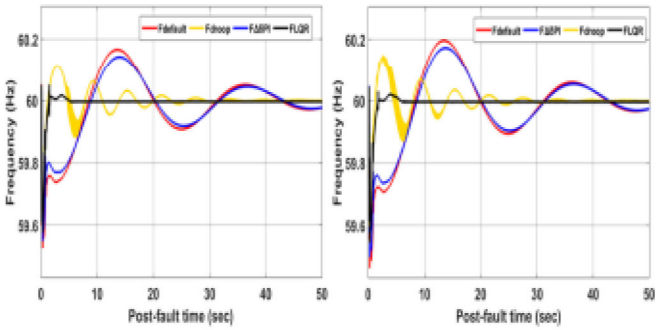

Fig. 11. Case I-A and I-B: Primary and secondary frequency response for various control approaches.

minimization-based PI control approach exhibits a frequency nadir of 59.56 Hz. The settling time for frequency was recorded at 66 s postfault for the default system. The proposed architecture settles the fastest in 5.84 s whereas the conventional frequency droop settles in 31.88 s and the $\Delta\delta$ minimization-based PI control settles in 63 s. To summarize case I-A, we can state that the proposed $\Delta\delta$ minimization-based approach performs a power-sharing based on the proximity of fault location to the source supporting frequency regulation. The frequency nadirs of the proposed approach and frequency droop approach are more or less similar. But the proposed approach settles the frequency fastest.

2) Fault Location 18 (Case I-B): For Case I-B, a fault is initiated on bus 18. The response recorded for the microgrids and the frequency responses for the default system, conventional frequency-droop, and $\Delta\delta$ based PI and LQR approach is detailed in Figs. 10 and 11. The effect of the fault on bus 18 is the least on the rate of change $\Delta\delta$ of bus 86 and the most on $\Delta\delta$ of bus 21. Consequently, the microgrid on bus 21 supplies the maximum 0.32 p.u. power whereas the microgrid at bus 86 commits the least of them with 0.2404 p.u. of peak power for

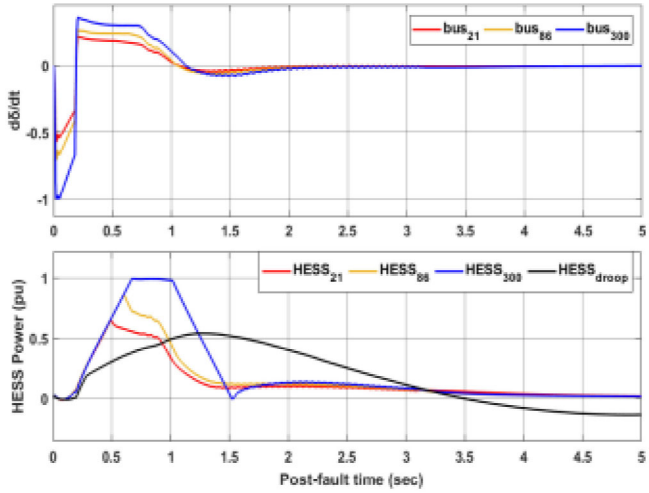

Fig. 12. Case II-A: DER HESS power sharing based on $\Delta\delta$ minimization.

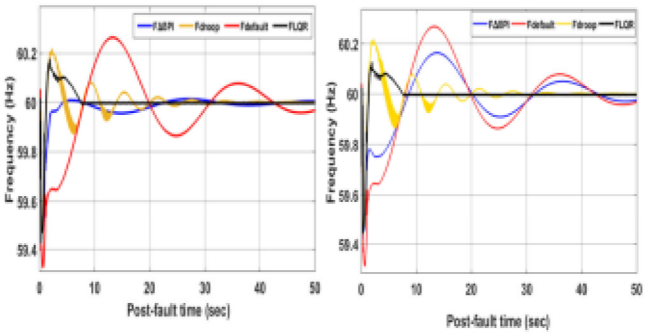

Fig. 13. Case II-A and II-B: (a) Primary and secondary frequency response. (b) DER HESS power sharing.

frequency regulation. After supporting the inertial response the proposed LQR approach gradually reduces the power contribution from all the microgrid as soon as the frequency reaches close of regulation. As a result of which the settling time for the secondary response is fastest within 6.92 s. Fig. 11 shows settling time for frequency for different approaches. The conventional frequency-droop approach settles second fastest in 29 s, whereas, the $\Delta\delta$ based PI control takes 62 s. The default system settling time due to synchronous generator inertia is 70 s.

3) Fault Location 67 (Case I-C): In this case, the microgrids at buses 86 and 300 experience a greater effect of the fault as compared to the microgrid on bus 21. However, this time the fault location is farther away from bus 21 than that in case II-B. As a result of this, the microgrid supplies 0.2 p.u. power while contributing to frequency regulation from bus 21. The maximum power of 0.34 p.u. and 0.29 p.u. is committed by buses to 86 and 300, respectively, due to their proximity to the fault location. Frequency nadir for the conventional frequency-droop approach shows the best result at 59.6 Hz, whereas that for the proposed approach improves to 59.54 Hz. Based on this result, the frequency-droop approach performs better for this case. However, the settling time for the proposed approach is recorded at 5.37 s whereas the frequency-droop approach settles 30 s later at 35 s. The default inertial response of the synchronous generator settles the slowest in 68 s postfault.

B. Frequency Response to LLLG Fault (Case II)

1) Fault Location 51 (Case II-A): Fig. 12 discusses the response of the three microgrids to the LLLG fault on bus 51. The first subplot shows the graphs of the rate of change of $\Delta\delta$ with respect to time on the individual microgrid buses. It can be observed that the $\Delta\delta$ shows the maximum change for bus 300 as a reaction to the LLLG fault. This is because bus 300 is closest to the fault location as compared to the other two buses. Thus, the microgrid connected at bus 300 supplies the maximum power of 0.99 p.u., as shown in Fig. 12. Microgrid at bus 86 is the next closest and supplies a peak power of 0.8522 p.u. on the base of the dispatch-able HESS, which is rated at 1700 kW. Microgrid at bus 21 is the farthest away and contributes 0.62 p.u. power to frequency regulation. As a result of frequency support from HESS, the frequency nadir improves to 59.48 Hz in comparison to 59.33 Hz for the default system response with the synchronous generator. The conventional frequency-droop approach results in a frequency nadir of 59.46 Hz. Whereas, the $\Delta\delta$ minimization-based PI control approach exhibits a frequency nadir of 59.44 Hz. The settling time for frequency was recorded 80 s postfault for the default system. The proposed architecture settles the fastest in 8 s whereas the conventional frequency droop settles at 32 s and the $\Delta\delta$ minimization-based PI control settles in 44 s. This is shown in Fig. 13. To summarize case II-A, we can state that the proposed $\Delta\delta$ minimization-based approach performs a power-sharing based on the proximity of fault location to the source supporting frequency regulation. The frequency nadirs of the proposed approach and frequency droop approach are more or less similar. But the proposed approach settles the frequency fastest.

2) Fault Location 18 (Case II-B): For Case II-B, an LLLG fault is initiated on bus 18. The response recorded for the microgrids and the frequency responses for the default system, conventional frequency-droop, and $\Delta\delta$ based PI and LQR approach is detailed in Figs. 12 and 13. The effect of the fault on bus 18 is the least on the rate of change $\Delta\delta$ of bus 86 and the most on $\Delta\delta$ of bus 21. Consequently, the microgrid on bus 21 supplies the maximum 0.9858 p.u. power whereas the microgrid at bus 86 commits the least of them with 0.6721 p.u. of peak power for frequency regulation. After supporting the inertial response the proposed LQR approach gradually reduces the power contribution from all the microgrid as soon as the frequency reaches close of regulation. As a result of which the settling time for the secondary response is fastest at 7.16 s. Fig. 13 shows settling time for frequency for different approaches. The conventional frequency-droop approach settles second fastest in 32 s, whereas, the $\Delta\delta$ based PI control takes 62 s. The default system settling time due to synchronous generator inertia is 78 s postfault.

3) Fault Location 67 (Case II-C): In this case, the microgrids at buses 86 and 300 experience a greater effect of the fault as compared to the microgrid on bus 21. However, this time the fault location is farther away from bus 21 than that in case II-B.

As a result of this, the microgrid supplies 0.536 p.u. power while contributing to frequency regulation from bus 21. The maximum power of 0.937 p.u. and 0.93 p.u. is committed by buses to 86 and 300, respectively, due to their proximity to the fault location. Frequency nadir for the proposed approach shows the best result at 59.49 Hz, whereas that for the frequency-droop approach improves to 59.45 Hz. Based on this result the performance for both approaches is comparable. However, the settling time for the proposed approach is recorded at 7.66 s postfault, whereas, the frequency-droop approach settles 22 s later in 29.42 s. The default inertial response of the synchronous generator settles the slowest in 76 s.

To summarize, it can be noted that the proposed approach does power-sharing based on fault proximity. The conventional frequency-droop approach shares power equally as it uses frequency, which is common throughout the distribution system. Frequency nadir is comparable for both approaches. However, the proposed approach has a faster settling time due to a more optimized power-sharing between microgrids that comes inherently with the approach. Table V showcases the result for the modified 123 bus system. The medium size test system performs well for all the cases with the proposed approach with the added advantage of fault proximity-based optimum power-sharing and faster settling time.

VII. Conclusion

This article highlights the advantages of the proposed control architecture and validates its real-time implementation and scalability on the modified IEEE 123 bus system. The proposed DER control topology enables dispatch-able operation using a three-phase load following GCI for improved inertial and secondary frequency response. The ancillary service for frequency regulation provided by the architecture only needs the rate of change of PCC angle to determine the contribution of the microgrid connected at PCC. It was observed that the proximity of DER from fault instance had an effect on the change in PCC angle ($\Delta\delta$) for each microgrid, and hence, coordinated management of multiple dc microgrids was possible through the proposed approach without the need of frequency-droop information of the system. The inertial response of both approaches was found to be comparable but the proposed architecture shows an improvement in the frequency settling response. Such architecture is favorable for multiple DERs connected in dc–ac topology due to the inherent power-sharing capability of the approach and also with the added advantage that the control signals of individual microgrids are invulnerable to external network dynamics.

References

[1] P. M. Diaz and H. J. El-Khozondar, "Electrical energy storage technologies and the application potential in power system operation: A mini review," in *Proc. IEEE 7th Palestinian Int. Conf. Elect. Comput. Eng.*, 2019, pp. 1–9.

[2] S. Vazquez, S. M. Lukic, E. Galvan, L. G. Franquelo, and J. M. Carrasco, "Energy storage systems for transport and grid applications," *IEEE Trans. Ind. Electron.*, vol. 57, no. 12, pp. 3881–3895, Dec. 2010.

[3] R. Abhinav and N. M. Pindoriya, "Grid integration of wind turbine and battery energy storage system: Review and key challenges," in *Proc. IEEE 6th Int. Conf. Power Syst.*, 2016, pp. 1–6.

[4] A. Chauhan and R. P. Saini, "Renewable energy based power generation for stand-alone applications: A review," in *Proc. Int. Conf. Energy Efficient Technol. Sustainability*, 2013, pp. 424–428.

[5] Y. Han, X. Ning, P. Yang, and L. Xu, "Review of power sharing, voltage restoration and stabilization techniques in hierarchical controlled dc microgrids," *IEEE Access*, vol. 7, pp. 149 202–149 223, 2019.

[6] H. Bevrani, A. Ghosh, and G. Ledwich, "Renewable energy sources and frequency regulation: Survey and new perspectives," *IET Renewable Power Gener.*, vol. 4, no. 5, pp. 438–457, 2010.

[7] H. Chen and Y. Kong, "Optimal spinning reserve for wind power integrated system using CVAR," in *Proc. IEEE Conf. Expo Transp. Electrific. Asia-Pac.* (ITEC Asia-Pac.), 2014, pp. 1–4.

[8] H. Yuhui, L. Dong, and L. Huaiqing, "Site and size selection strategies of energy storage system based on power supply and storage capability index," in *Proc. Int. Conf. Renewable Power Gener.*, 2015, pp. 1–6.

[9] F. Matthey *et al.*, "Cost-benefit analysis tool and control strategy selection for lithium-ion battery energy storage system," in *Proc. IEEE Power Energy Soc. Gen. Meeting*, 2015, pp. 1–5.

[10] I. Alsaidan, A. Khodaei, and W. Gao, "Determination of battery energy storage technology and size for standalone microgrids," in *Proc. IEEE Power Energy Soc. Gen. Meeting*, 2016, pp. 1–5.

[11] B. Das and A. Kumar, "Optimal sizing and selection of energy storage system considering load uncertainty," in *Proc. 2nd Int. Conf. Power, Energy Environment: Towards Smart Technol.*, 2018, pp. 1–9.

[12] M. S. Mahdavi, G. B. Gharehpetian, P. Ranjbaran, and H. Azizi, "Frequency regulation of aut microgrid using modified fuzzy PI controller for flywheel energy storage system," in *Proc. 9th Annu. Power Electron., Drives Syst. Technol. Conf.*, 2018, pp. 426–431.

[13] S. Ghosh and S. Kamalasadan, "An energy function-based optimal control strategy for output stabilization of integrated DFIG-flywheel energy storage system," *IEEE Trans. Smart Grid*, vol. 8, no. 4, pp. 1922–1931, Jul. 2017.

[14] I. Calero, C. A. Cañizares, and K. Bhattacharya, "Compressed air energy storage system modeling for power system studies," *IEEE Trans. Power Syst.*, vol. 34, no. 5, pp. 3359–3371, Sep. 2019.

[15] K. V. Vidyanandan and N. Senroy, "Frequency regulation in microgrid using wind—fuel cell—diesel generator," in *Proc. IEEE Power Energy Soc. Gen. Meeting*, 2012, pp. 1–8.

[16] S. Kamalasadan and C. M. Tanton, "Modeling and simulation of PEM fuel cell generator as a micro grid," in *Proc. IEEE Ind. Appl. Soc. Annu. Meeting*, 2010, pp. 1–8.

[17] C. Romaus, J. Bocker, K. Witting, A. Seifried, and O. Znamenshchykov, "Optimal energy management for a hybrid energy storage system combining batteries and double layer capacitors," in *Proc. IEEE Energy Convers. Congr. Expo.*, 2009, pp. 1640–1647.

[18] T. Thomas and M. K. Mishra, "Control strategy for a PV-wind based standalone dc microgrid with hybrid energy storage system," in *Proc. IEEE 1st Int. Conf. Energy, Syst. Inf. Process.*, 2019, pp. 1–6.

[19] U. Akram and M. Khalid, "A coordinated frequency regulation framework based on hybrid battery-ultracapacitor energy storage technologies," *IEEE Access*, vol. 6, pp. 7310–7320, 2018.

[20] J. Rocabert, R. Capó-Misut, R. S. Muñoz-Aguilar, J. I. Candela, and P. Rodriguez, "Control of energy storage system integrating electrochemical batteries and supercapacitors for grid-connected applications," *IEEE Trans. Ind. Appl.*, vol. 55, no. 2, pp. 1853–1862, Mar./Apr. 2019.

[21] G. Deshpande and S. Kamalasadan, "An approach for micro grid management with hybrid energy storage system using batteries and ultra capacitors," in *Proc. IEEE PES General Meeting—Conf. Expo.*, 2014, pp. 1–5.

[22] P. Cairoli and R.A. Dougal, "New horizons in dc shipboard power systems: New fault protection strategies are essential to the adoption of dc power systems," *IEEE Electrific. Mag.*, vol. 1, no. 2, pp. 38–45, Dec. 2013.

[23] X. Zeng, T. Liu, S. Wang, Y. Dong, and Z. Chen, "Comprehensive coordinated control strategy of PMSG-based wind turbine for providing frequency regulation services," *IEEE Access*, vol. 7, pp. 63 944–63953, 2019.

[24] P. C. Nakka and M. K. Mishra, "Droop characteristics based damping and inertia emulation of dc link in a hybrid microgrid," *IET Renewable Power Gener.*, vol. 14, no. 6, pp. 1044–1052, 2020.

[25] Y. Fu, Y. Wang, and X. Zhang, "Integrated wind turbine controller with virtual inertia and primary frequency responses for grid dynamic frequency support," *IET Renewable Power Gener.*, vol. 11, no. 8, pp. 1129–1137, 2017.

[26] Z. Peng, J. Wang, D. Bi, Y. Dai, and Y. Wen, "The application of microgrids based on droop control with coupling compensation and inertia," *IEEE Trans. Sustain. Energy*, vol. 9, no. 3, pp. 1157–1168, Jul. 2018.
[27] K. W. Joung, T. Kim, and J. Park, "Decoupled frequency and voltage control for stand-alone microgrid with high renewable penetration," *IEEE Trans. Ind. Appl.*, vol. 55, no. 1, pp. 122–133, Jan./Feb. 2019.
[28] U. Datta, A. Kalam, and J. Shi, "Battery energy storage system control for mitigating PV penetration impact on primary frequency control and state-of-charge recovery," *IEEE Trans. Sustain. Energy*, vol. 11, no. 2, pp. 746–757, Apr. 2020.
[29] Y. Li, L. He, F. Liu, C. Li, Y. Cao, and M. Shahidehpour, "Flexible voltage control strategy considering distributed energy storages for dc distribution network," *IEEE Trans. Smart Grid*, vol. 10, no. 1, pp. 163–172, Jan. 2019.
[30] X. Li, Z. Li, L. Guo, J. Zhu, Y. Wang, and C. Wang, "Enhanced dynamic stability control for low-inertia hybrid ac/dc microgrid with distributed energy storage systems," *IEEE Access*, vol. 7, pp. 91 234–91 242, 2019.
[31] A. Joshi, A. Suresh, and S. Kamalasadan, "Control and dispatch of distributed energy resources with improved frequency regulation using fully active hybrid energy storage system," in *2020 IEEE Int. Conf. Power Electron., Smart Grid Renewable Energy*, 2020, pp. 1–6.
[32] M. Davari and Y. A. I. Mohamed, "Robust vector control of a very weak-grid-connected voltage-source converter considering the phase-locked loop dynamics," *IEEE Trans. Power Electron.*, vol. 32, no. 2, pp. 977–994, Feb. 2017.
[33] P. Wang, J. Xiao, L. Setyawan, C. Jin, and C. F. Hoong, "Hierarchical control of active hybrid energy storage system (HESS) in dc microgrids," in *Proc. 9th IEEE Conf. Ind. Electron. Appl.*, 2014, pp. 569–574.
[34] W. H. Kersting, "Radial distribution test feeders," in *Proc. IEEE Power Eng. Soc. Winter Meeting. Conf.*, Jan. 2001, vol. 2, pp. 908–912.

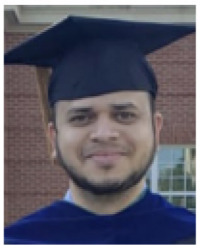

Aniket Joshi (Student Member, IEEE) received the bachelor's degree in electrical engineering from the University of Pune, Pune, India, in 2013 and the M.Sc. and Ph.D. degrees in electrical engineering from the University of North Carolina, Charlotte, NC, USA, in 2016 and 2021, respectively.

He is currently an Associate Scientist with the ABB Corporate Research Center, Raleigh, NC, USA. His research interests include microgrids, smart inverters, hybrid energy storage systems, and optimal control.

Arun Suresh (Student Member, IEEE) received the B.Tech. degree in electrical engineering from the Mahatma Gandhi University, New Delhi, India, in 2012 and the M.Tech. degree in electrical engineering from Kerala University, Thiruvananthapuram, India, in 2015. He is currently working toward the Ph.D. degree in electrical engineering with the University of North Carolina, Charlotte, NC, USA.

His research interests include power system stability and control, smart grid, integrated transmission and distribution systems.

Sukumar Kamalasadan (Senior Member, IEEE) received the B.Tech. degree in electrical and electronics engineering from the University of Calicut, Kerala, India, in 1991, the M.Eng. degree in electrical power systems management from the Asian Institute of Technology, Bangkok, Thailand, in 1999, and the Ph.D. degree in electrical engineering from the University of Toledo, Toledo, OH, USA, in 2004.

He is currently a Professor with the Department of Electrical and Computer Engineering, University of North Carolina at Charlotte,Charlotte, NC, USA. His research interests include intelligent and autonomous control, power systems dynamics, stability and control, smart grid, microgrid, and real-time optimization, and control of power system.

Dr. Kamalasadan was the recipient of the several awards including the NSF CAREER Award and IEEE Best Paper Award.